Citation
Yuan, C. and Chen, W. and Pham, T.M. and Hao, H. and Jian, C. and Shi, Y. 2019. Strain rate effect on interfacial bond behaviour between BFRP sheets and steel fibre reinforced concrete. Composites Part B: Engineering. 174: ARTN 107032. http://doi.org/10.1016/j.compositesb.2019.107032

Strain Rate Effect on Interfacial Bond Behaviour between BFRP Sheets and Steel Fibre Reinforced Concrete

Cheng Yuan[1], Wensu Chen[1]*, Thong M. Pham[1], Hong Hao[1]*, Cui Jian[2], Yanchao Shi[2]

[1]*Centre for Infrastructural Monitoring and Protection, School of Civil and Mechanical Engineering, Curtin University, Australia*
[2]*Tianjin University and Curtin University Joint Research Center of Structure Monitoring and Protection, School of Civil Engineering, Tianjin University, China*
**Corresponding Author*

Abstract

Numerous studies have shown that using steel fibre reinforced concrete (SFRC) and retrofitting with Fibre-reinforced polymer (FRP) composites can improve the strength and ductility of RC structures against impact and explosive loadings. The interface between FRP and concrete has been identified as one of the weakest parts of the FRP strengthened structures subjected to dynamic loading, with debonding failure usually observed as the primary failure mode. In order to properly analysis and design of FRP strengthened reinforced concrete (RC) structures, it is important to understand the dynamic bonding strength between FRP and concrete. An experimental investigation regarding to the dynamic interfacial bond behaviour between basalt fibre (BFRP) sheets and SFRC is carried out in this study. Concrete prisms were made of short steel fibres with three volumetric fractions (i.e. V_f = 0.5%, 1.0%, and 1.5%) to improve the tensile strengths. To achieve different strain rates, the loading velocities varied from 8.33E-6 m/s, 0.1 m/s, 1 m/s, 3 m/s, to 8 m/s. Experimental results show the bond strength and bond-slip were sensitive to strain rate. The loading rate changed the debonding failure modes from concrete substrate failure to interfacial debonding. In addition, the shear resistance of the interface increased with the fibre volume under both quasi-static and dynamic loadings. Based on the testing data, an empirical bond-slip model,

incorporating the volumetric fraction of steel fibre and strain rate, is established for FRP-strengthened SFRC structures.

Keywords: Dynamic loading; Strain rate; BFRP; SFRC; Interfacial bond behaviour.

1. Introduction

Using steel fibre reinforced concrete (SFRC) and fibre-reinforced polymer (FRP) is effective to improve the strength and ductility of reinforced concrete (RC) members. As reported by Mutalib and Hao [1], FRP strengthening is effective in enhancing RC slab's capacity to resist blast loads. Saatcioglu et al. [2] experimentally and numerically examined the responses of FRP-strengthened RC members and found that FRP strengthening was effective in enhancing blast resistance. Field blast tests on RC slabs and SFRC panels were conducted by Lan et al. [3] and found that adding fibres in concrete mix improved the damage resistance. Lee et al. [4] conducted blast tests on blast-damaged specimens retrofitted with steel fibres reinforced cementitious composite (SFRCC) as well as CFRP sheets and reported that the addition of steel fibres resulted in improved ductility and enhanced blast resistance. For the CFRP-strengthened specimens, the flexural capacity and ductility were enhanced and the debonding failure of CFRP was observed.

FRP debonding is a premature failure mode for FRP-strengthened RC structures when subject to different loading conditions [5-8]. Normally only 30% - 40% of FRP strength could be utilized due to the premature debonding failure. The FRP debonding cannot be easily prevented due to the localized cracks of concrete [9-11]. Steel fibres can be used to improve the interfacial bond behaviour since the addition of steel fibres can improve the cracking resistance. Compared with plain concrete, SFRC shows better ductility due to its enhanced tensile strength. Additionally, the mechanical properties of concrete were significantly influenced by the volume fraction and aspect ratio of fibres. [12, 13]. Due to the advantages of SFRC and FRP, numerous studies investigated the FRP-strengthened fibres reinforced concrete (FRC) structures [14-17]. Experimental studies conducted by Li et al. [14] found that hybrid FRP-strengthened FRC beams with 0.9% short steel fibres and 0.1% polymer fibres yielded higher bending stiffness and crack resistance. GFRP debonding induced by the flexural cracks was observed in their tests. Experimental and numerical studies conducted by Yin and Wu [15] found that FRP-strengthened SFRC beams with four steel fibre volumetric fractions (i.e. 0, 0.25%, 0.5%, and 1%) exhibited a higher load bearing capacity, higher concrete toughness, and greater fracture energy. By conducting numerical studies o, Benvenuti and Orlando [18] found that the flexural capacity was significantly improved and the ductility of the post-peak branch was remarkably enhanced for FRP-strengthened SFRC beams. Gribniak et al. [17] reported that the ultimate deformation increased by 20% for FRP-strengthened SFRC beams ass compared to the control specimen.

FRC has been widely utilized to repair damaged RC elements while FRP composites have been used to strengthen defective structures. The efficiency of strengthening is primarily determined by the bonding performance. As FRP debonding has been observed in many tests, e.g., the field blast tests conducted by Lee et al. [4], it is necessary to quantitatively study dynamic interfacial bond behaviour between FRP and FRC at different strain rates. So far, very limited studies have been conducted to investigate the strain rate effect on the interfacial bond behaviour between FRP and concrete, and all these studies are limited to relatively low strain rates with the highest strain rate reached being around 4.9 s^{-1} [19-21]. This low strain rate does not necessarily reflect the true dynamic behaviour of FRP-retrofitted structures under high strain rates generated by high-speed impact and blast load, under which the strain rate of structural response can reach approximately up to a few hundred per second [22]. In addition, the study on the interfacial bond behaviour between FRP and SFRC is very limited. Yuan et al. [23] experimentally investigated the interfacial bond of BFRP-to-SFRC joint and the found that the bond-slip relationship was sensitive to steel fibre volume under quasi-static loading. However, studies of dynamic bonding behaviours between FRP and SFRC have not been available in the literature yet.

To better understand the effect of steel fibre on the dynamic interfacial bond behaviour between FRP and SFRC, different fibre volumetric fractions have been considered in the experimental program. To achieve high strain rate, single-lap shear tests with various loading speeds up to 8 m/s were carried out. Experimental results including strain distribution, bond strength, and bond-slip response are presented and discussed in this paper. An empirical dynamic bond-slip model incorporating the fibre volume and the strain rate is proposed and validated.

2. Experimental program

2.1 Material properties

Concrete prisms with dimension of 150 x 150 x 300 mm were prepared for single-lap shear tests. The 28-day mechanical properties of concrete including compressive and tensile strengths are given in Table 1. Four volumetric fractions of steel fibres (i.e. 0%, 0.5%, 1.0% and 1.5%) were used for the concrete with the design grade of 30 MPa. The short steel fibres with the fibre-reinforcing index ($V_f L_f/\phi_f$) in the range of 0 to 1.25 were used in the experimental program. The Young's modulus, tensile strength, and density of steel fibres provided by the supplier are 200 GPa, 2.5 GPa, and 7,800 kg/m^3, respectively.

Table 1. Mechanical properties of SFRC

Specimen ID	Volume fraction V_f (%)	Fibre-reinforcing index ($V_f L_f / \phi_f$)	Compressive strength $f_c^{'}$ (MPa)	Splitting tensile strength f_t (MPa)
PC-1			29.48	2.71
PC-2	0	0	30.18	2.98
PC-3			28.74	2.86
Mean			29.47	2.85

			(COV=0.02)	(COV=0.05)
SFRC-0.5-1			31.33	2.97
SFRC-0.5-2	0.50	0.417	33.05	3.16
SFRC-0.5-3			32.90	3.21
Mean			32.43	3.11
			(COV=0.03)	(COV=0.04)
SFRC-1.0-1			32.59	3.33
SFRC-1.0-2	1.00	0.833	34.09	3.58
SFRC-1.0-3			33.48	3.41
Mean			33.39	3.44
			(COV=0.02)	(COV=0.04)
SFRC-1.5-1			33.72	3.93
SFRC-1.5-2	1.50	1.250	34.24	3.86
SFRC-1.5-3			32.39	3.57
Mean			33.45	3.79
			(COV=0.03)	(COV=0.05)

In this study, unidirectional BFRP sheets with an area density of 300 g/m^2 were prepared in this study. The tested rupture tensile strength, elastic modulus, and failure strain of the BFRP sheets were 1,333 MPa, 73 GPa, and 0.12%, respectively. The adhesive used to saturate the BFRP sheets was two-component epoxy resins at a ratio of 5:1. The ultimate tensile strength, elastic modulus, and rupture strain of the adhesive provided by the supplier were 50.5 MPa, 2.8 GPa, and 4.5%, respectively [24].

2.2 Test matrix

Dynamic single-lap shear tests were carried out using an INSTRON® VHS 160-20 high speed servo hydraulic testing machine, as shown in Figure 1 (a). This machine can provide a constant loading velocity at the range of 0.1 m/s to 25 m/s. The fast jaw of this machine speeds up to a desired loading velocity and firmly grab the specimen then hold it at the desired velocity until the final debonding of the BFRP-to-concrete joints. A steel jig was designed to hold the concrete prisms in place to prevent the out-of-plane movement. As shown in Figure 1 (b), the bond length and width of BFRP sheets of all the specimens were 200 mm and 40 mm, respectively. To prevent the edge effect of the concrete prisms, 50 mm unbonded region prior to the loaded end was reserved, as shown in Figure 1 (b).

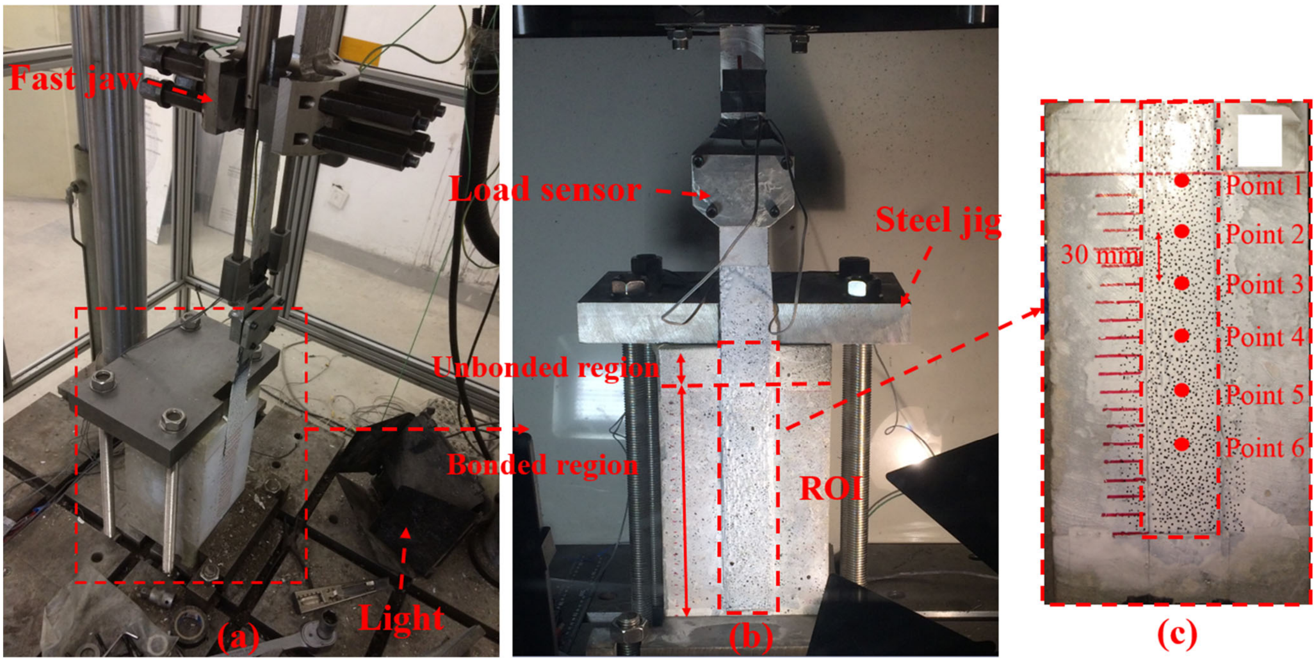

Note: *ROI* is the region of interest

Figure 1. (a) Test setup; (b) Specimen detail; and (c) Tracking points

A total of 56 single-lap shear specimens were prepared for this study. The GOM Correlate© 2D-DIC software was used in this study to conduct the DIC analysis. The successive digital images during testing were recorded first by using a high-speed camera and then processed in the DIC software to obtain the displacement and strain values. Six points were selected as the tracking points to determine the dynamic stress equilibrium and bond-slip curves, as shown in Figure 1 (c). Table 2 presents the specimen details and experimental results of the static and dynamic tests. The single-lap shear specimen ID was named as "*QSX-n*" and" *DX-m-n*". "*QSX* or *DX*" refers to the quasi-static (QS) or dynamic (D) single-lap shear tests with steel fibre volumetric fraction of *X*%. The letter "*m*" stands for the dynamic loading velocity. The letter "*n*" means the specimen number.

Table 2. Specimen details and experimental results

Specimen ID	**Volume fraction V_f (%)**	***RI* (V_fL_f/ϕ_f)**	**Loading velocity (m/s)**	**Strain rate (s^{-1})**	***Pu* (kN)**	**ε_m (%)**	**τ_m (MPa)**	**s_o (mm)**	**G_f (N/mm)**	**Failure mode**
QS0-1	0	0	8.33E-6	2.50E-05	7.87	1.10	2.2	0.131	1.10	C
QS0-2	0	0	8.33E-6	2.50E-05	6.93	0.99	2.11	0.146	0.86	C
QS0.5-1	0.5	0.417	8.33E-6	2.50E-05	8.09	1.09	2.79	0.138	1.17	C

QS0.5-2	0.5	0.417	8.33E-6	2.50E-05	8.11	1.12	2.57	0.145	1.17	C
QS1-1	1.0	0.833	8.33E-6	2.50E-05	8.12	1.14	2.68	0.143	1.18	C
QS1-2	1.0	0.833	8.33E-6	2.50E-05	8.36	1.17	3.02	0.137	1.25	C
QS1.5-1	1.5	1.250	8.33E-6	2.50E-05	8.26	1.17	3.05	0.139	1.22	C
QS1.5-2	1.5	1.250	8.33E-6	2.50E-05	9.19	1.19	3.45	0.147	1.51	C
D0-0.1-1	0	0	0.1	4.51	8.07	1.18	3.25	0.13	1.16	C
D0-0.1-2	0	0	0.1	4.31	7.88	1.09	2.95	0.141	1.11	C
D0-0.1-3	0	0	0.1	4.21	7.67	1.08	2.68	0.135	1.05	C
D0-1-1	0	0	1.0	25.9	8.34	1.45	4.81	0.132	1.24	C
D0-1-2	0	0	1.0	-	-	-	-	-	-	-
D0-1-3	0	0	1.0	29.56	9.72	1.48	4.2	0.128	1.69	C
D0-3-1	0	0	3.0	65.12	10.51	1.65	5.34	0.124	1.97	C
D0-3-2	0	0	3.0	-	-	-	-	-	-	-
D0-3-3	0	0	3.0	60.75	11.18	1.69	6.31	0.121	2.23	C/CE
D0-8-1	0	0	8.0	173.55	12.01	1.82	9.44	0.107	2.57	C/CE
D0-8-2	0	0	8.0	155.55	11.89	1.78	9.05	0.098	2.52	C/CE
D0-8-3	0	0	8.0	150.75	13.5	1.83	9.82	0.112	3.25	C/CE
D0.5-0.1-1	0.5	0.417	0.1	2.11	9.14	1.44	4.67	0.135	1.49	C
D0.5-0.1-2	0.5	0.417	0.1	2.52	8.79	1.27	4.07	0.112	1.38	C
D0.5-0.1-3	0.5	0.417	0.1	1.62	8.34	1.20	4.16	0.153	1.24	C
D0.5-1-1	0.5	0.417	1.0	13.83	8.91	1.49	4.58	0.172	1.42	C
D0.5-1-2	0.5	0.417	1.0	16.06	9.53	1.51	5.73	0.111	1.62	C
D0.5-1-3	0.5	0.417	1.0	-	-	-	-	-	-	-
D0.5-3-1	0.5	0.417	3.0	76.55	11.34	1.70	7.75	0.167	2.29	C/CE
D0.5-3-2	0.5	0.417	3.0	64.93	10.42	1.71	8.49	0.166	1.94	C
D0.5-3-3	0.5	0.417	3.0	68.81	11.89	1.69	8.14	0.126	2.52	C/CE
D0.5-8-1	0.5	0.417	8.0	134.91	12.13	1.80	9.95	0.139	2.62	C/CE
D0.5-8-2	0.5	0.417	8.0	131.73	12.41	1.84	8.97	0.144	2.75	C/CE
D0.5-8-3	0.5	0.417	8.0	148.87	12.53	1.93	9.77	0.135	2.80	C/CE
D1-0.1-1	1.0	0.833	0.1	2.75	9.9	1.35	6.72	0.138	1.75	C
D1-0.1-2	1.0	0.833	0.1	2.07	9.12	1.34	5.47	0.129	1.48	C
D1-0.1-3	1.0	0.833	0.1	4.17	8.07	1.29	4.65	0.124	1.16	C
D1-1-1	1.0	0.833	1.0	28.09	9.32	1.46	6.35	0.125	1.55	C
D1-1-2	1.0	0.833	1.0	15.38	9.61	1.51	6.69	0.14	1.65	C
D1-1-3	1.0	0.833	1.0	27.93	9.87	1.53	7.23	0.146	1.74	C
D1-3-1	1.0	0.833	3.0	41.8	9.89	1.70	9.14	0.112	1.74	C
D1-3-2	1.0	0.833	3.0	43.95	12.25	1.72	8.16	0.126	2.68	C/CE
D1-3-3	1.0	0.833	3.0	61.49	11.69	1.71	8.84	0.13	2.44	C
D1-8-1	1.0	0.833	8.0	164.12	12.43	1.79	8.79	0.107	2.76	C/CE
D1-8-2	1.0	0.833	8.0	130.13	13.39	1.87	8.58	0.112	3.20	C/CE
D1-8-3	1.0	0.833	8.0	137.74	12.66	1.78	9.12	0.124	2.86	C/CE
D1.5-0.1-1	1.5	1.250	0.1	2.09	9.46	1.44	6.4	0.136	1.60	C
D1.5-0.1-2	1.5	1.250	0.1	2.16	9.49	1.45	5.98	0.12	1.61	C
D1.5-0.1-3	1.5	1.250	0.1	1.61	8.25	1.20	5.17	0.139	1.21	C
D1.5-1-1	1.5	1.250	1.0	29.44	12.01	1.63	8.85	0.141	2.57	C
D1.5-1-2	1.5	1.250	1.0	16.29	11.39	1.60	7.61	0.131	2.31	C
D1.5-1-3	1.5	1.250	1.0	23.03	11.25	1.51	8.09	0.132	2.26	C
D1.5-3-1	1.5	1.250	3.0	49.83	11.33	1.72	9.83	0.109	2.29	C
D1.5-3-2	1.5	1.250	3.0	38.21	11.66	1.73	9.78	0.11	2.43	C/CE
D1.5-3-3	1.5	1.250	3.0	42.28	12.86	1.78	9.98	0.117	2.95	C/CE
D1.5-8-1	1.5	1.250	8.0	167.54	13.3	1.97	8.58	0.102	3.16	C/CE
D1.5-8-2	1.5	1.250	8.0	129.46	12.97	1.87	8.76	0.112	3.00	C/CE
D1.5-8-3	1.5	1.250	8.0	160.61	12.32	1.80	9.34	0.108	2.71	C/CE

Note: RI represents the fibre-reinforcing index as indicated in Figure 1; *C* means debonding in concrete layer; *CE* is the interface debonding between concrete and epoxy; and "-" means unavailable data.

3. Experimental results and discussions

Experimental results from the impact single-lap shear tests are only valid when the equilibrium condition is achieved. The equilibrium condition was checked carefully in this study and only those results which satisfy this condition are included. Details of the analysis on the equilibrium and validity of the tests are presented in Section 3.2.

3.1 Failure modes and debonding load

Debonding of BFRP sheets associated with concrete debris was observed in all the tested specimens under both quasi-static and dynamic loadings. For all the test specimens, debonding location changed from concrete layers to interface of concrete-epoxy with the increase of loading rates. During the process of debonding, debris of coarse aggregates, mortar and steel fibres with the detachment of FRP sheets can also be observed, as shown in Figure 2 (a), (b) , and (c). Additionally, with the volumetric fraction of steel fibres increasing, more steel fibres were pulled out from the matrix. The typical debonding failure modes of the tested specimens are shown in Figure 2 (d) and (e). It is observed that the additional steel fibres had a marginal effect on the debonding mechanism for the BFRP-SFRC interface. However, the debonding mechanism changed with the debonding location from the concrete layer (*C*) to the interface between concrete and epoxy (*CE*) with the loading rate increasing, as shown in Figure 2 (d) and (e). This might be because the tensile strength of FRC concrete is enhanced significantly with the rising strain rate while the strain rate has a marginal effect on the strength of epoxy resin [25, 26]. At a low loading rate, the specimen has enough time to initiate the internal defects and develop the cracks through the weak zone in the concrete substrate. However, at a high loading rate, the concrete strength is enhanced due to the strain rate effect, and at the same time the specimen has no enough time to extend the cracks through the concrete substrate. Therefore the failure extends along the concrete-adhesive interface for the single-lap shear test.

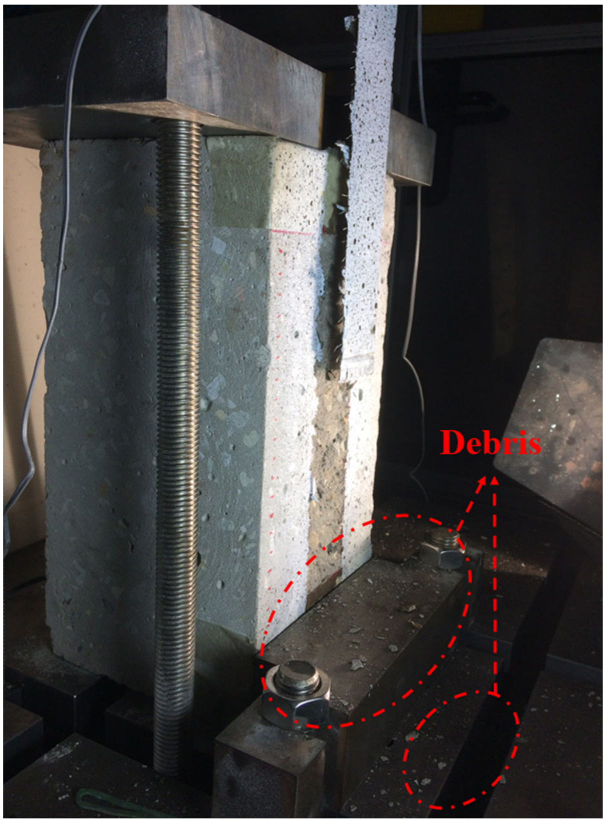

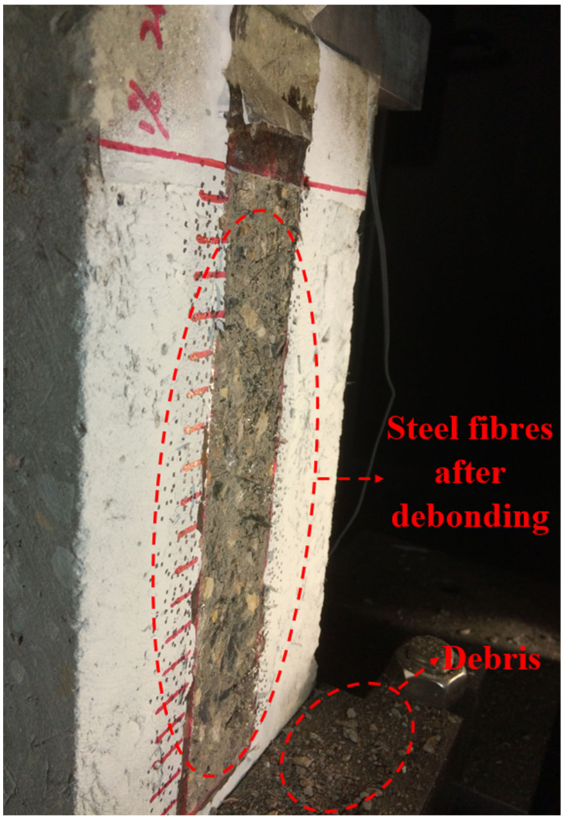

(a) Plain concrete debris after testing (QS0-3-1) (b) SFRC debris after testing (D1-3-1)

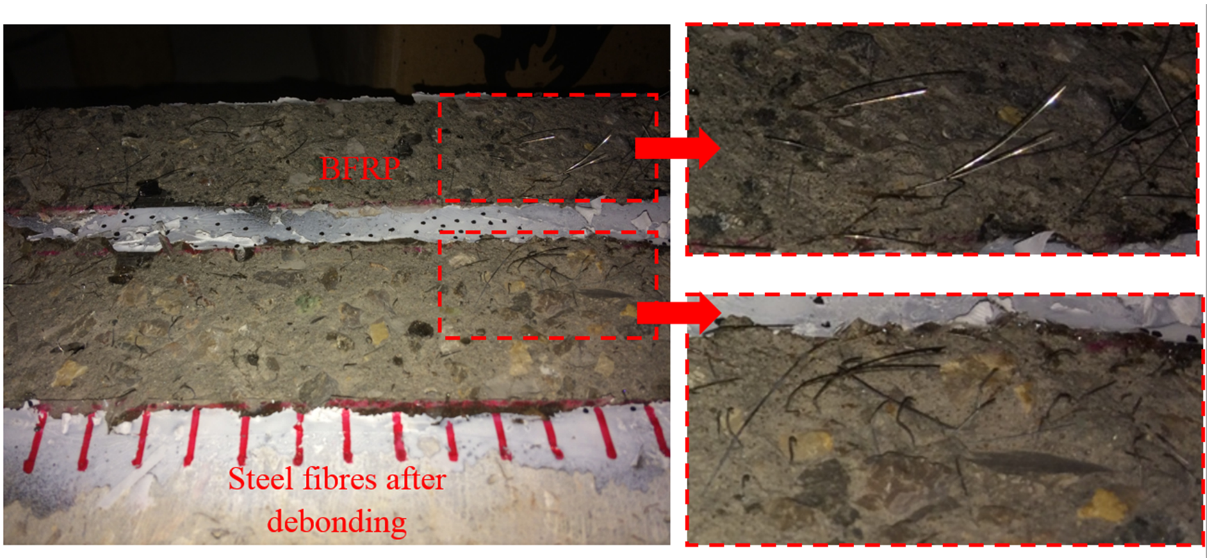

(c) Pull-out of steel fibres for D1-1-1 after testing

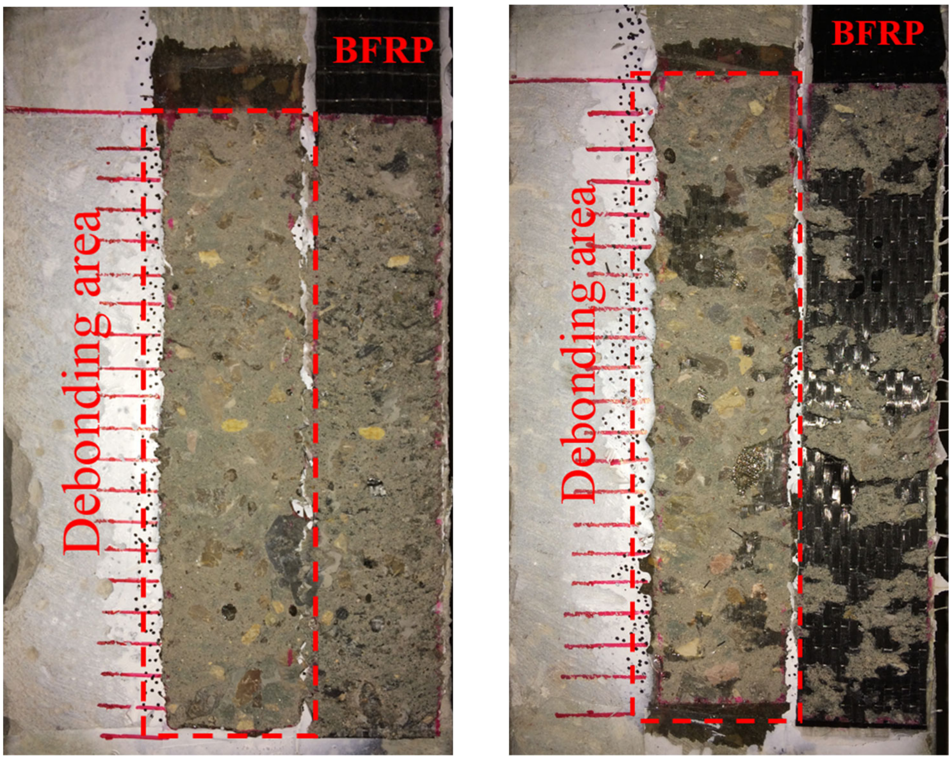

(d) Failure mode of (L) QS0-1 and (R) D0-8-1

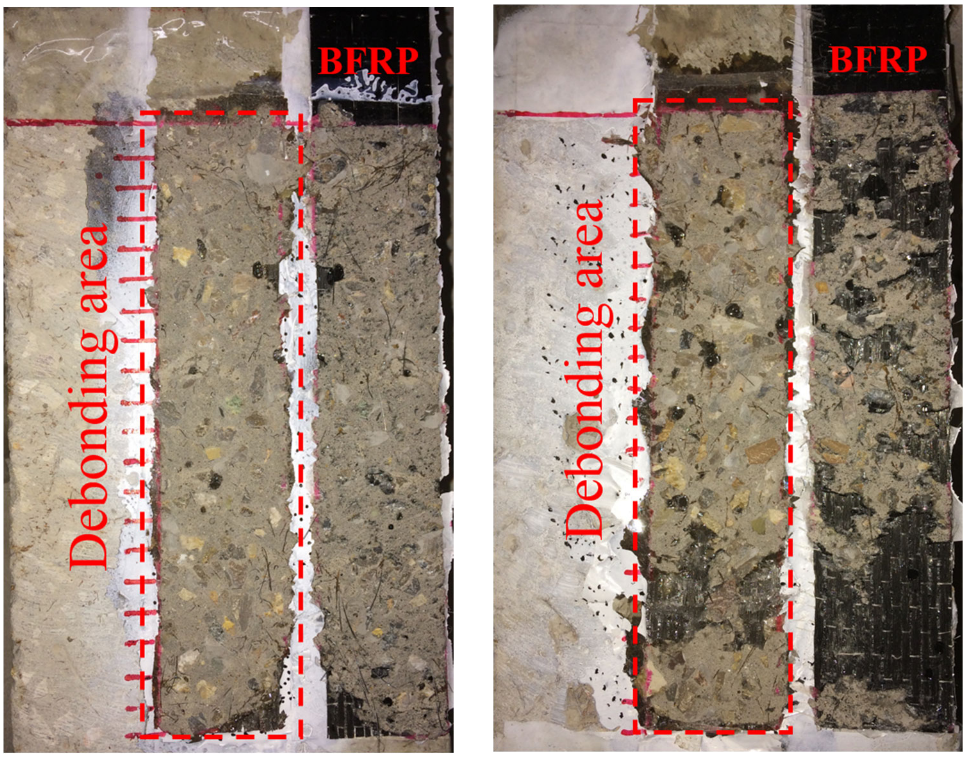

(e) Failure mode of (L) QS1-1 and (R) D1-8-1

Figure 2. Photograph of failure modes

Figure 3 shows the impact of steel fibre volume on the debonding loads under different loading rates. The general trend of the test results shows that the debonding load increased with fibre volume as well as the loading speed. The increased debonding load is caused by the enhanced tensile strength of concrete with the fibre volume increasing. For example as the volume increased from 0% to 1.5%, the debonding load increased by 15.2 % from 7.87 kN to 9.07 kN at the loading speed of 0.1 m/s.

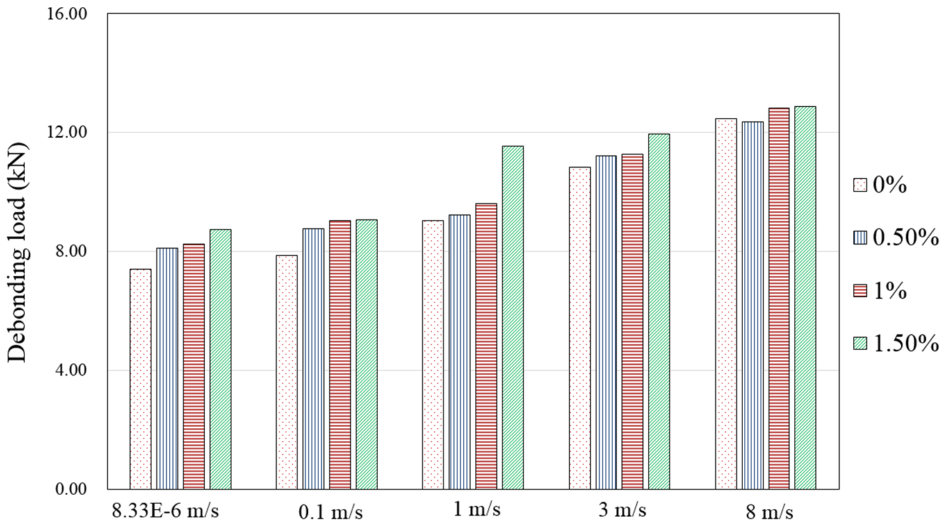

Figure 3. Debonding load under various loading rates

3.2 Strain time curves and stress equilibrium

Figure 4 plots the strain contours at different loading rates. The strain contour consists of different colours, red colour refers to the maximum strain while dark blue colour represents the minimum strain. The strain contours show the strain distributions at different loading stages under various loading velocities. At the initial stage of loading (i.e 0.4*P*), a large local strain gradient in red colour was seen near the loaded end. With the tensile load increasing, the localized zone in red colour continued to develop and propagated along the BFRP sheets and a transition zone in colours of yellow and green formed. The distance of the strain transition zone is known as the stress transfer zone, which increased slightly due to the added steel fibres but decreased with the loading rate increasing. The added steel fibres and strain rate had a marginal impact on the pattern of strain distribution.

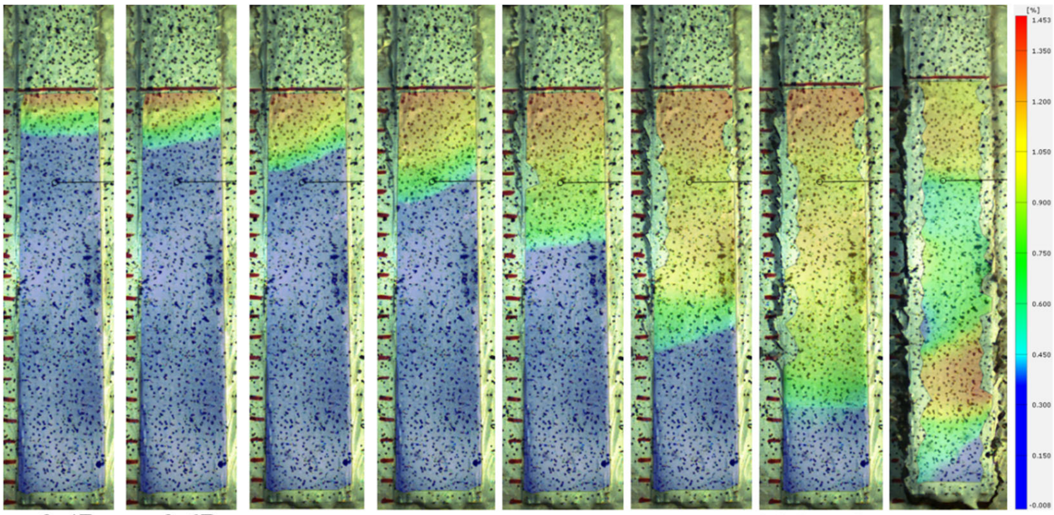

(a) D0.5-0.1-1

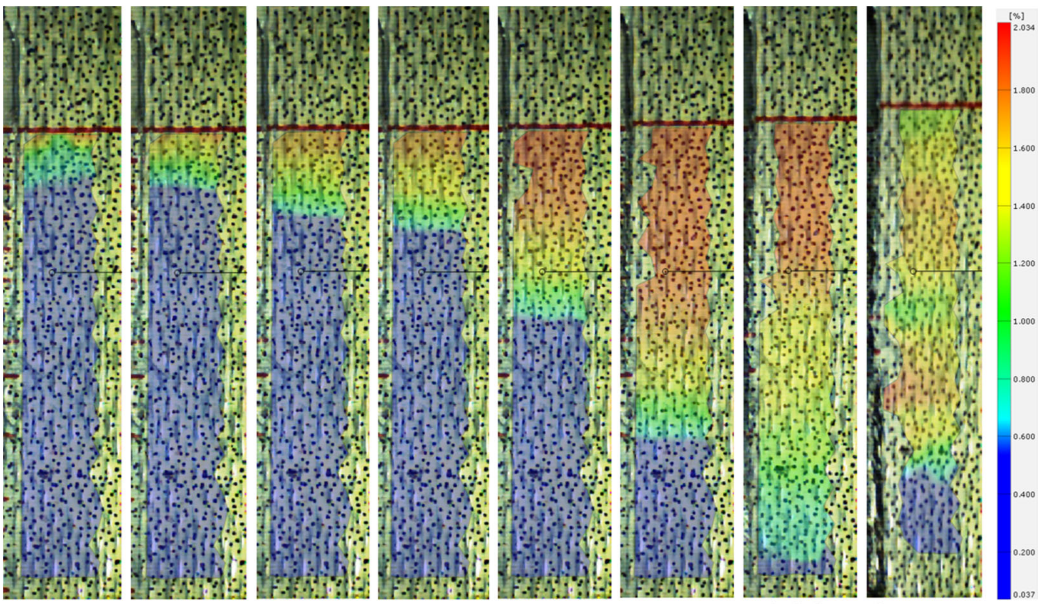

(b) D1.5-8-1

Figure 4. Strain contours at the loading velocities

Figure 5 illustrates the strain time histories of the tested specimens at the loading velocities of 0.1 m/s and 8 m/s. Six points along the BFRP sheets in the bonded region were selected as the tracking points, as shown in Figure 1 (c). It is found that the strain vs. time curves are steeper under higher loading velocity than the case under lower loading velocity. Additionally, the ultimate debonding strain increased with the steel fibre volume under both the quasi-static and dynamic tests. The higher debonding strain of BFRP sheets was resulted from the enhanced shear resistance of the BFRP-to-concrete interface.

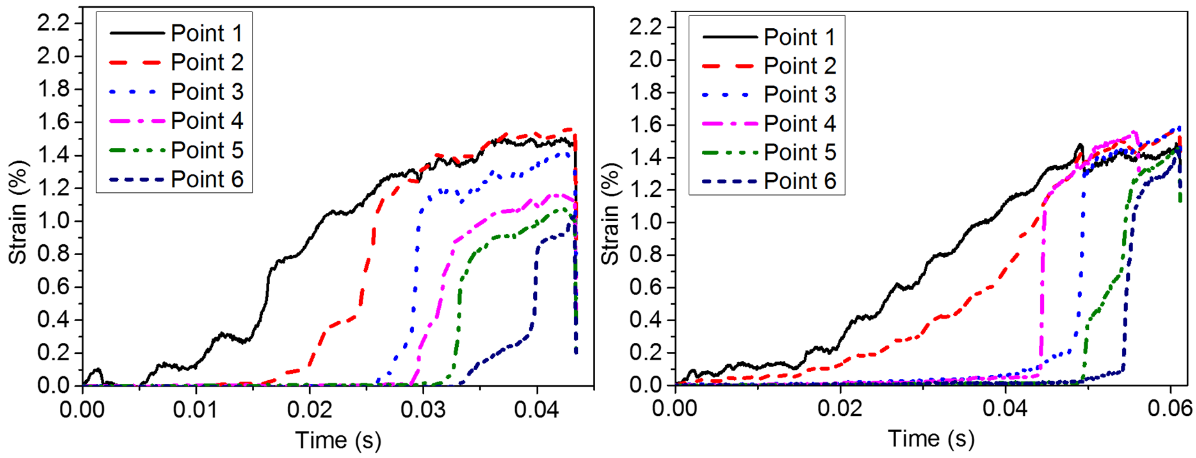

(a) D0.5-0.1-1 (b) D1.5-0.1-1

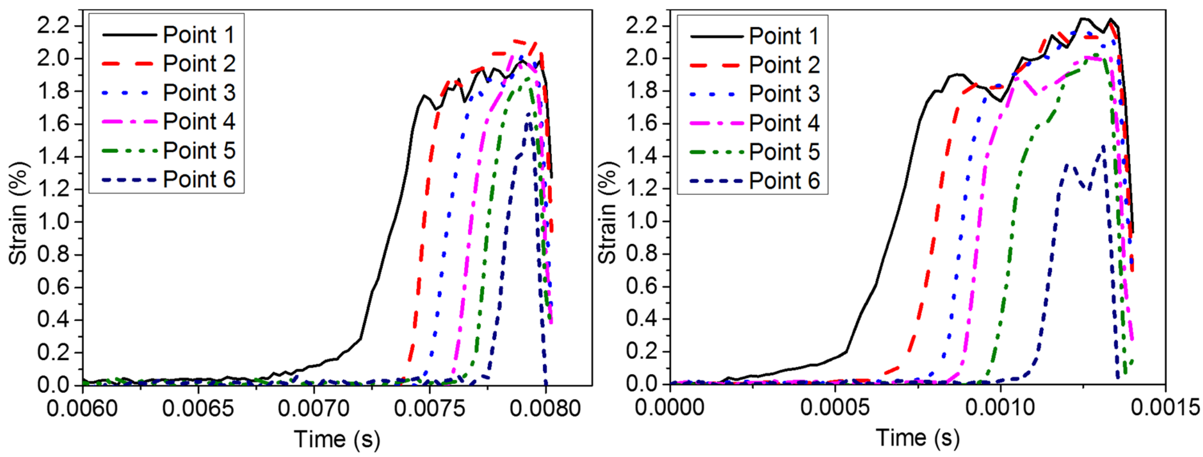

(c) D0.5-8-1 (d) D1.5-8-1

Figure 5. Strain-time histories

To check the validity of the experimental results, the dynamic stress equilibrium must be achieved in the dynamic test [27, 28]. For the quasi-static single shear tests, the loading rate of 0.5 mm/min allows the stress wave to travel forth and back many times inside the interface to obtain the stress equilibrium. To validate the dynamic stress equilibrium, six points along the centreline of BFRP sheets in the bonded region were selected to compare the strain distributions at different loading stages (Figure 1 (c)). As shown in Figure 5, the strain distributions obtained from the six selected points show very similar shape and value. The strain of BFRP sheets almost reached the plateau indicating the uniform strain distribution and thus uniform stress or stress equilibrium condition was achieved. It should be noted that Point 1 and Point 6 have slightly different strain distributions from other points. It is because Point 1 is located at the boundary of unbonded and bonded regions where the stress redistributes and Point 6 is close to the free end where the full debonding behaviour cannot develop due to the brittle debonding process [29].

In addition, Figure 6 illustrates the strain rate distributions along the BFRP sheets at different time instants. The strain rate was obtained by the differentiation of strain time history using $\dot{\varepsilon}=\frac{d\varepsilon}{dt}$. A bell-shape strain rate propagation along the BFRP sheets can be observed for all the test specimens. The strain rate increased with the loading speed and the strain rate for D1-1-1 was 28.09 s^{-1} at the loading velocity of 1 m/s and the strain rate for D1.5-8-1 was 167.54 s^{-1} at the loading velocity of 8 m/s. All the tested specimens show the similar strain rate distribution along the bonding length and the testing results are summarized Table 2.

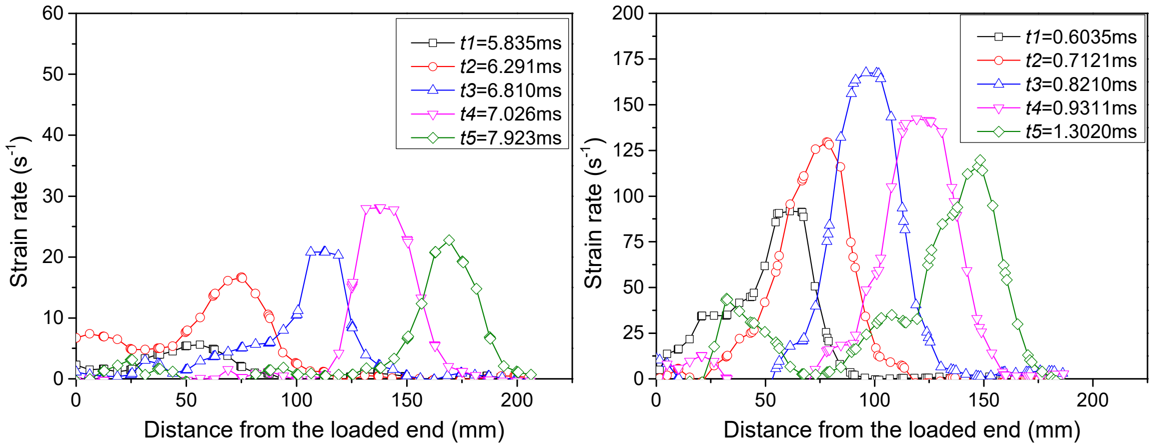

(a) D1-1-1 (b) D1.5-8-1

Figure 6. Strain rate distribution at different loading velocities

Figure 7 illustrates the local shear stress distribution. Four different loading levels after the initial debonding load were selected to obtain a robust shear stress distribution. With the applied load increasing, the peak value of the shear stress gradually propagated to the free end. Due to the shear stress concentration near the loaded end, a relatively higher shear stress was observed and then the shear stress maintained approximately constant with the debonding propagation. The shear stress increased significantly with the strain rate but increased slightly with the fibre volume. As compared to Specimen D0.5-0.1-1, the average PSS of Specimen D0.5-8-1 increased by 113% when the strain rate increased from 2.11 s^{-1} to 131.73 s^{-1}. Compared to the strain rate effect, the effect of fibre volume on the PSS was relatively small. There was a 37% increment in the PSS at the same loading speed of 0.1 m/s when the fibre volume increased from 0.5% to 1.5%.

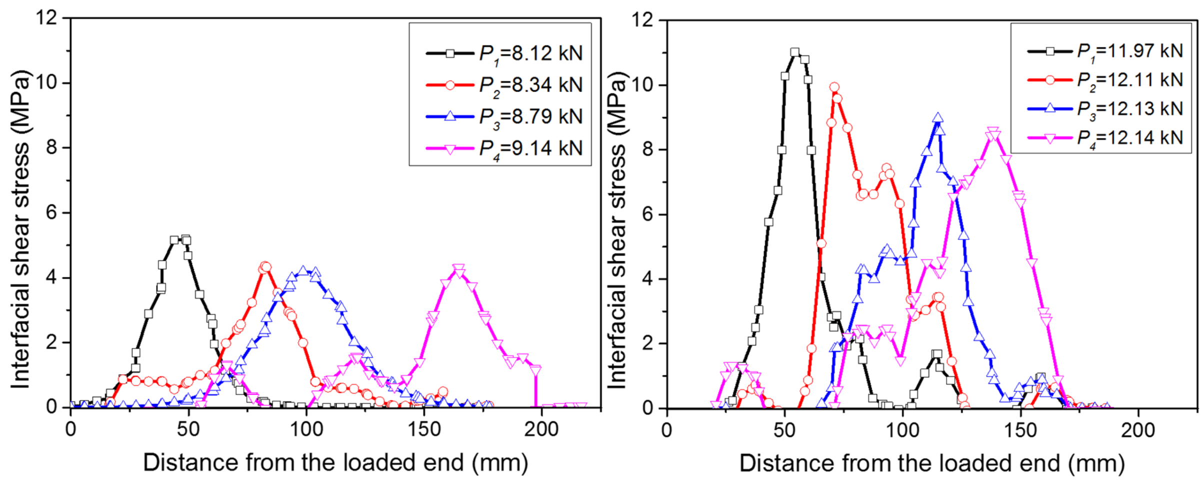

(a) D0.5-0.1-1 (b) D0.5-8-1

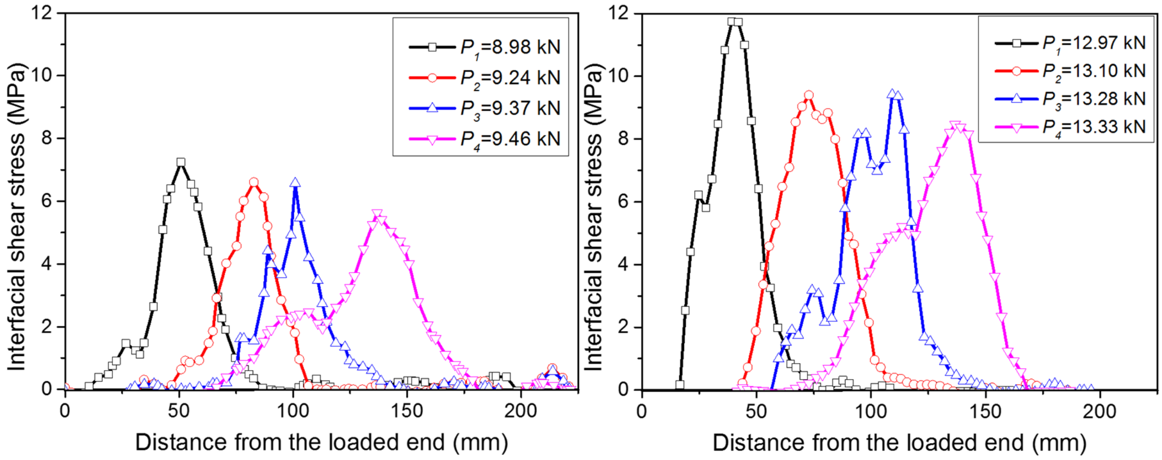

(c) D1.5-0.1-1 (d) D1.5-8-1

Figure 7. Local shear stress distribution

3.3 Experimental bond-slip curves

The DIC technique was used to measure the BFRP strain distributions and the relative slip, which can be used to obtain the interfacial bond-slip curves. The reliability of this technique as compared to readings from strain gauges was verified in the previous studies [23, 30]. Figure 8 and Figure 9 illustrate the typical bond-slip curves with different steel fibre volumes under various loading rates. The following equations can be used to obtain the interfacial shear stress and shear slip based on the measured strain distributions [31]:

$$\tau(x) = E_f t_f \frac{d\varepsilon}{dx} \tag{1}$$

$$s(x) = \int \varepsilon dx \tag{2}$$

where $\tau(x)$ is the interfacial shear stress, E_f is the elastic modulus, t_f is the thickness of BFRP sheet, $d\varepsilon/dx$ is the strain gradient, $s(x)$ is the shear slip along the BFRP sheets, and ε is the strain measured by the DIC technique.

Figure 8 and Figure 9 illustrate the bond-slip relationships of each specimen under four loading levels and the peak shear stress (PSS) of each specimen is obtained from the mean value at four different loading levels after the initial debonding load. The distance of 85 mm, 115 mm, 145 mm, and 175 mm shown in the legend refer to the range of strain distributing at the four different loading levels after the initial debonding load. It is observed that the bond-slip curves for PCs and SFRCs under quasi-static and dynamic loadings exhibit the similar trend, i.e. non-linear ascending and descending branches [32]. With the shear slip increasing, the reduction of shear stress was observed. Figure 8 illustrates the effect of steel fibre volume on the bond-slip response under quasi-static loading and the results show that the interfacial PSS increased with fibre volume. Figure 9 shows the effect of strain rate on the bond-slip response for Specimen D0.5 under different loading rates. It is clear that the PSS increased significantly with strain rate. Compared with the effect of fibre volume, the impact of strain rate on the interfacial shear stress is more significant.

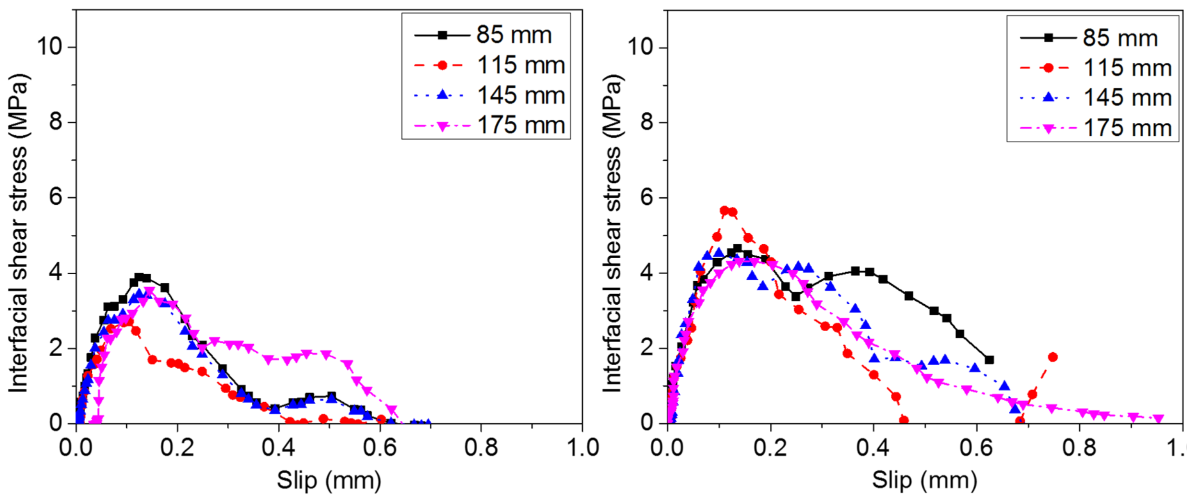

(a) QS0-1 (b) QS0.5-1

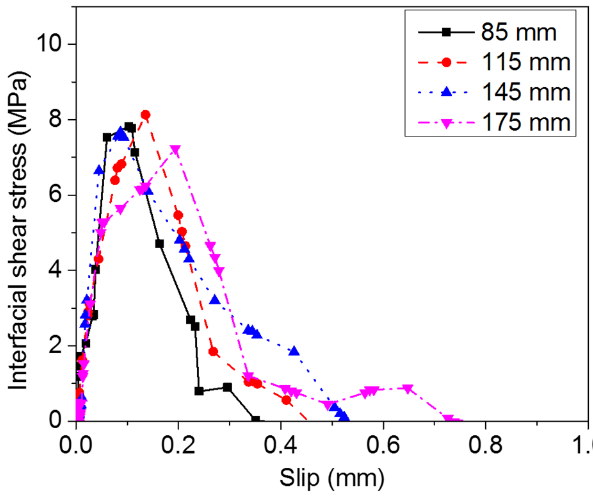

(c) QS1-1

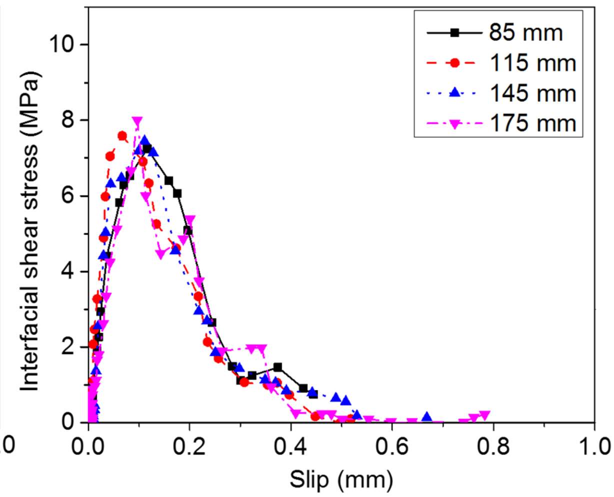

(d) QS1.5-1

Figure 8. The relationship between peak shear stress and fibre volume under quasi-static loading

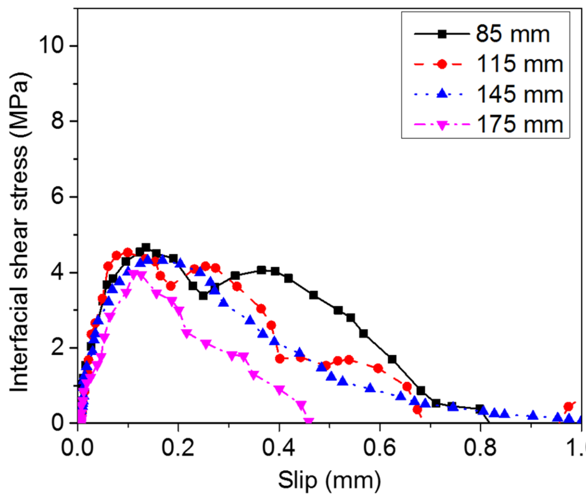

(a) D0.5-0.1-1

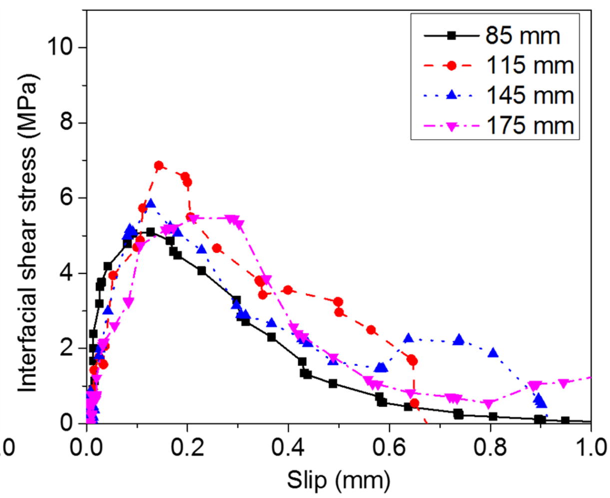

(b) D0.5-1-1

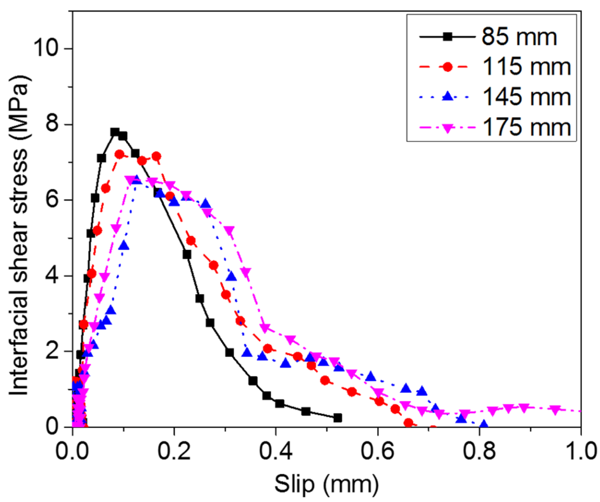

(c) D0.5-3-1

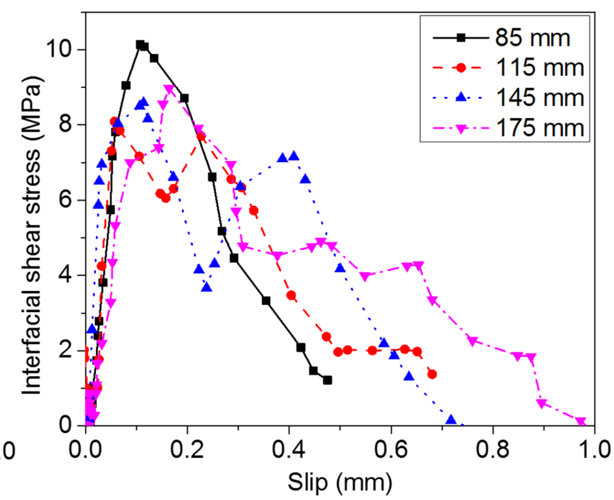

(d) D0.5-8-1

Figure 9. The relationship between peak shear stress and loading speed under different dynamic loadings

3.4 Effect of steel fibres on the interfacial bond

Figure 10 illustrates the influence of steel fibre volumetric fraction on the BFRP-concrete interface bond behaviour. It is found that the average debonding load, the interfacial fracture energy (IFE), the ultimate debonding strain, and the PSS increased with the steel fibre volume. As compared to the control group (PC), the average debonding loads of the specimens with volumetric fraction of 0.5%, 1%, and 1.5% increased by 9.46%, 11.35%, and 17.91% at quasi-static loading, and increased by 3.43%, 3.98%, and 10.19% at dynamic loading rate of 3 m/s, respectively. Due to the bridging action of fibres in the matrix, the fracture area of BFRP-to-SFRC is relatively larger than that of BFRP-to-PC. In this study, the tensile strength of concrete increased with the steel fibre volume, which is consistent with the previous study [33]. The increased tensile strength of concrete leads to the increased interfacial fracture energy. As compared to the quasi-static tests, the specimens with 0%, 0.5%, 1% and 1.5% fibre volume at the dynamic loading speed of 8 m/s experienced the increment of average PSS by 338%, 257%, 210%, and 174 % and the average IFE increased by 184%, 133%, 142%, and 117%, respectively. It should be noted that the interfacial PSS increased with the rising strain rate in general while the PSS stopped rising over the loading speed of 3 m/s for the case of 1.5% fibre volume. It might be due to the strain fluctuation caused by the system ringing under relatively high loading speed (i.e. 8 m/s) because the shear stress was derived from the strain profile. For instance, the obtained shear stress was averaged from the shear stress at four different locations (i.e. 85 mm, 115 mm, 145 mm and 175 mm), which show the variations of PSS as shown in Figure 9 (d).

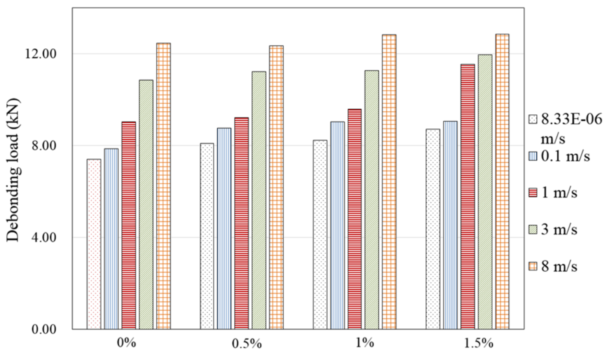

(a) Average debonding load

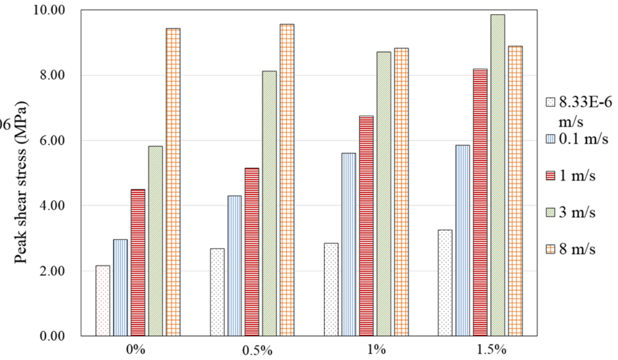

(b) Average peak shear stress

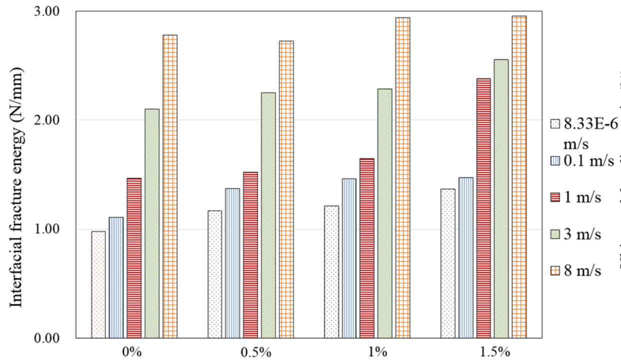

(c) Average interfacial fracture energy

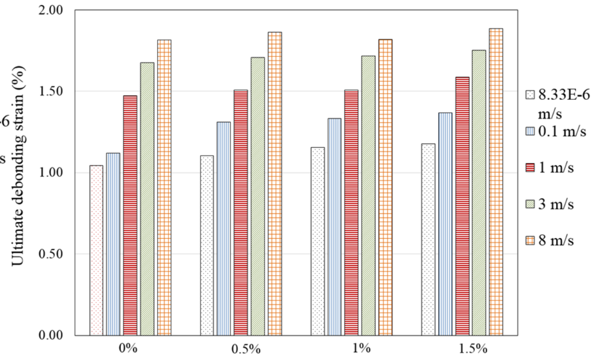

(d) Average ultimate debonding strain

Figure 10. Effect of steel fibre volume under different loading rates

3.5 Effect of strain rate on the bond behaviour

As given in Table 2, the debonding load, the ultimate debonding strain, the IFE, and the PSS are strain rate dependent for both the BFRP-to-PC and BFRP-to-SFRC interfaces. For the modelling purpose in the following section, the dynamic increase factors (DIF) against the corresponding strain rate for the IFE (G_f) and PSS (τ_m) are proposed and plotted in Figure 11. A bilinear relationship between the obtained DIF and strain rate is presented in logarithmic functions. It is observed that the increments of IFE and PSS are not significant when the strain rate is less than 3 s^{-1} while the increment becomes more apparent when the strain rate is great than 3 s^{-1}. This is because both the plain concrete (PC) and SFRC are strain rate dependent materials and the tensile strength increases with the strain rate, especially when the strain rate is higher than 3 s^{-1} [34, 35].

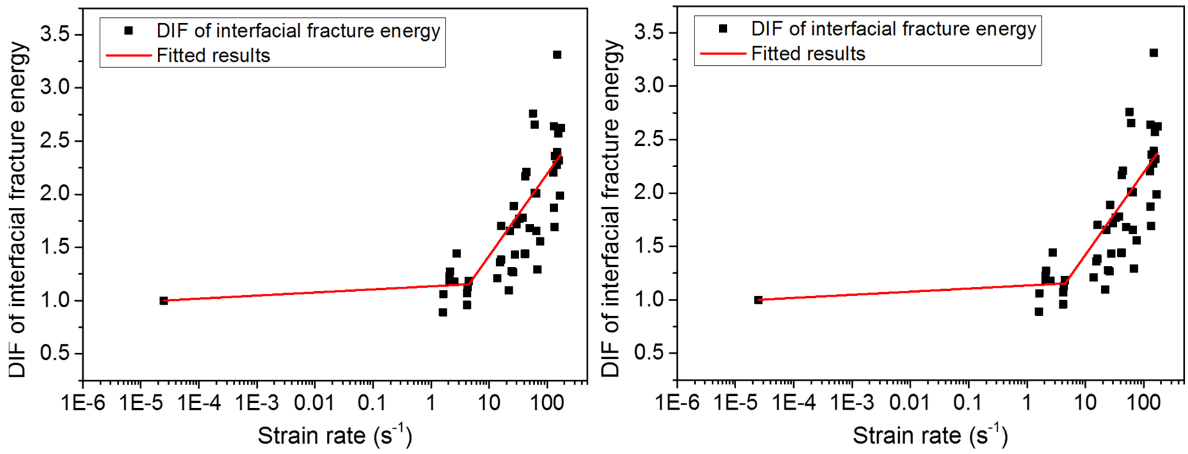

(a) Interfacial fracture energy (b) Peak shear stress

Figure 11. DIF vs. strain rate

Based on the testing data, the following empirical equations are proposed for predicting the dynamic values by substituting the obtained DIF into the proposed model of IFE and PSS.

For dynamic interfacial fracture energy:

$$DIF_{G_f} = 0.0291\log(\dot{\varepsilon}) + 1.135, \text{ when } 2.5\times10^{-5}s^{-1} \le \dot{\varepsilon} \le 3s^{-1} \tag{3}$$

$$DIF_{G_f} = 0.9001\log(\dot{\varepsilon}) + 0.358, \text{ when } 3s^{-1} \le \dot{\varepsilon} \le 173.55s^{-1} \tag{4}$$

For dynamic interfacial PSS:

$$DIF_{\tau_m} = 0.1257\log(\dot{\varepsilon}) + 1.629, \text{ when } 2.5\times10^{-5}s^{-1} \le \dot{\varepsilon} \le 3s^{-1} \tag{5}$$

$$DIF_{\tau_m} = 1.2049\log(\dot{\varepsilon}) + 0.8, \text{ when } 3s^{-1} \le \dot{\varepsilon} \le 173.55s^{-1} \tag{6}$$

where DIF_{Gf} and $DIF_{\tau m}$ are respectively dynamic increase factor (*DIF*) of IFE G_f and PSS τ_m, and $\dot{\varepsilon}$ is strain rate.

4. Analytical investigation and the proposed model

4.1 Dynamic bond-slip relationship

Figure 12 (R) illustrates the typical bond-slip curves for the tested specimens. It is observed that all the tested specimens exhibited an approximately triangular shape with a linear ascending stage before the PSS, and after that a non-linear descending stage is observed until the final debonding [36-38]. A linear equation can be used to depict the ascending stage, and an exponential function can be used to describe the descending stage. As shown in Figure 12 (L), three stages can be defined in the strain-slip curves: (1) linear; (2) nonlinear; and (3) constant [39, 40]. These three stages from the strain-slip curves can derive the corresponding three parts in the local bond-slip curves as shown in Figure 12 (R).

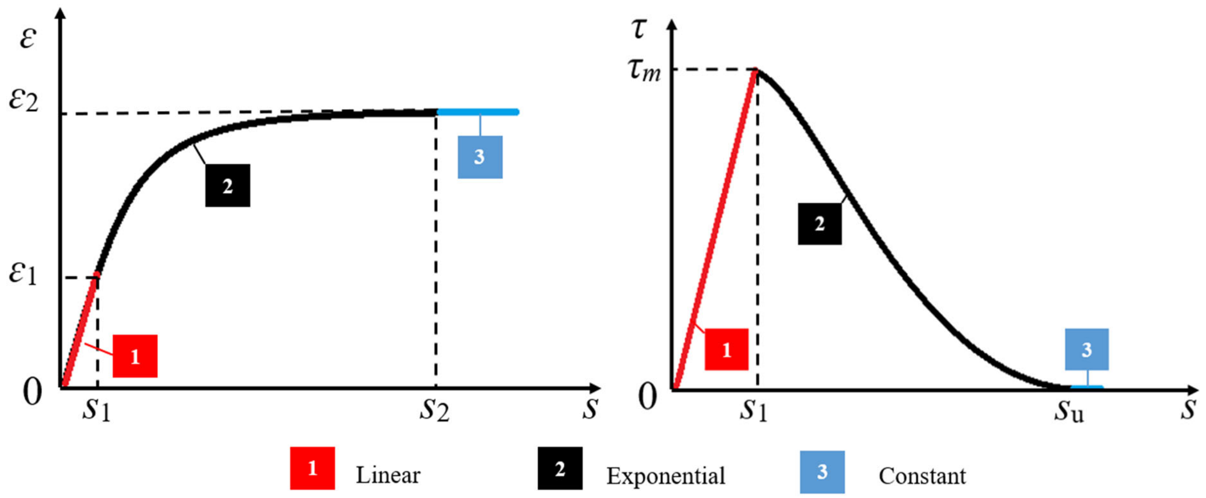

Figure 12. Determination of the bond-slip curve (L) Strain-slip curve; (R) Bond-slip curve

Based on the determined shape of the bond-slip curve in Figure 12 (R), the shear stress can be expressed as follows [29]:

$$\tau(s)=\begin{cases}\tau_m\left(\dfrac{s}{s_1}\right) & s\le s_1\\ \tau_m e^{-\omega(s-s_1)} & s_1\le s\le s_u\\ 0 & s_u\le s\end{cases} \tag{7}$$

where $\tau(s)$ is the shear stress, τ_m is the PSS, s_1 is the maximum elastic slip, and s is the shear slip.

The IFE G_f is defined as the enclosed area of the bond-slip curve for the FRP-to-concrete interface, the following expression can be used to calculate the interfacial fracture energy:

$$G_f = \int_0^{+\infty} \tau ds = \int_0^{s_1} \tau ds + \int_{s_1}^{+\infty} \tau ds \tag{8}$$

By integrating the shear stress and the slip, the IFE can be determined as follows:

$$G_f = \frac{1}{2}\tau_m s_1 + \int_{s_1}^{+\infty} \tau_m e^{-\omega(s-s_1)} ds = \frac{1}{2}\tau_m s_1 + \frac{\tau_m}{\omega} \tag{9}$$

The coefficient ω can be expressed by [41]:

$$\omega = \frac{\tau_m}{G_f - \frac{1}{2} s_1 \tau_m} \tag{10}$$

Therefore, the bond-slip model can be characterized by some key parameters (i.e. τ_m, s_1, s_u, and ω). It can be found that these key parameters can be determined by the interfacial fracture energy (G_f). Once these key parameters are determined, the dynamic bond-slip relationship can be obtained.

4.2 Interfacial fracture energy

The IFE (G_f) is represented as the enclosed area of the bond-slip curve. However, due to the fluctuation of the obtained bond-slip curves, inaccurate interfacial fracture energy might be derived when using the bond-slip curves. Therefore, the IFE is obtained from the debonding load in this study, as follows [42, 43]:

$$G_f = \frac{P_u^2}{2 b_f^2 t_f E_f} \tag{11}$$

The models to predict IFE have been proposed and adopted in numerous studies. It was reported that the interfacial fracture energy increases with the higher tensile strength of concrete. For SFRC, the splitting tensile strength increased with steel fibre volume, but the added steel fibres had slight effect on the compressive strength. Thus, the formula to calculate the tensile strength of SFRC by incorporating the fibre-reinforcing index ($V_f L_f/\phi_f$) can be expressed as follows [13]:

$$f_t = 0.516\left(f'_{cu}\right)^{0.5} + 0.101\left(f'_{cu}\right)^{0.5}\left(\frac{V_f L_f}{\phi_f}\right) + 0.199\left(\frac{V_f L_f}{\phi_f}\right) \tag{12}$$

For the BFRP-PC interface under quasi-static loading, it is found that the IFE correlates well with the FRP-to-concrete width ratio (β_w) and tensile strength of concrete (f_t) [44]. In addition, the debonding failure shifted from concrete layer to epoxy-concrete interface and fracture of epoxy was also observed under high loading speed (i.e. 8 m/s). Thus, the contribution of epoxy on the IFE should be taken into account [45]. The tensile strain energy of epoxy $\frac{f_a^2}{2E_a}$, which is represented as the area under the tensile stress-strain curves of the epoxy was incorporated into the proposed model. The testing data from the existing studies [20, 46-49] and the testing data from this study were employed to conduct the regression analysis. Table 3 summarizes the specimen details and the test results. Therefore, the empirical model based on the best-fit coefficients can be obtained as follows:

$$G_{f,S}\left(PC\right) = 0.55\beta_w^{\,2}\left(\frac{f_e^2}{2E_e}\right)^{0.42}\sqrt{f_t} \tag{13}$$

Table 3. Summary and comparison of testing data

Reference	Specimen ID	Test method	Adhesive			FRP			Concrete	$P_{u,exp}$ (kN)
			f_a (MPa)	E_a (GPa)	$f_a^2/2E_a$ (N/mm^2)	Ef (GPa)	tf (mm)	bf (mm)	f_t (MPa)	
Present study	QS1-1	Single shear	50.50	2.8	0.455	73	0.24	40	2.85	7.87

	QS1-2		50.50	2.8	0.455	73	0.24	40	2.85	6.93
Shen et al. [46]	1-1	Double shear	45.80	2.6	0.403	105	0.121	50	2.62	11.40
	1-2		45.80	2.6	0.403	105	0.121	50	2.62	10.80
	1-3		45.80	2.6	0.403	105	0.121	50	2.62	13.60
Huo et al. [20]	C50-1-1	Beam	65	3.2	0.660	236	0.169	50	2.89	13.60
	C50-1-2		65	3.2	0.660	236	0.169	50	2.89	11.50
	C50-2-1		65	3.2	0.660	236	0.338	50	2.89	18.00
	C50-2-2		65	3.2	0.660	236	0.338	50	2.89	14.20
	C80-2-1		65	3.2	0.660	236	0.338	80	2.89	17.50
	C80-2-2		65	3.2	0.660	236	0.338	80	2.89	18.40
Toutanji et al. [47]	AA-1	Single shear	23.6	4.1	0.068	110	0.495	50	2.73	7.56
	AA-2		23.6	4.1	0.068	110	0.66	50	2.73	9.29
	AA-3		23.6	4.1	0.068	110	0.825	50	2.73	11.64
	AA-4		23.6	4.1	0.068	110	0.99	50	2.73	12.86
	BB-1		23.6	4.1	0.068	110	0.495	50	2.73	12.55
	BB-2		23.6	4.1	0.068	110	0.66	50	2.73	14.25
	BB-3		23.6	4.1	0.068	110	0.825	50	2.73	17.72
	BB-4		23.6	4.1	0.068	110	0.99	50	2.73	18.86
	CC-1		23.6	4.1	0.068	110	0.495	50	2.73	13.24
	CC-2		23.6	4.1	0.068	110	0.66	50	2.73	15.17
	CC-3		23.6	4.1	0.068	110	0.825	50	2.73	18.86
	CC-4		23.6	4.1	0.068	110	0.99	50	2.73	19.03
Yun et al. [48]	M-EB	Double shear	54	3.0	0.289	257	0.66	50	3.03	26.30
Yun and Wu [49]	N30-0-1	Single shear	45	3.5	0.289	235	0.167	50	2.81	23.7
	N30-0-2		45	3.5	0.289	235	0.167	50	2.81	24.4
	N45-0-1		45	3.5	0.289	235	0.167	50	3.22	27.7
	N45-0-2		45	3.5	0.289	235	0.167	50	3.22	27.4

The IFE increased with the steel fibre volume. Therefore, the fibre-reinforcing index ($V_f L_f/\phi_f$) was set as a factor to determine the IFE of the BFRP-SFRC interface. Based on the best-fitted coefficients through regression analysis, the relationship between the IFE and fibre-reinforcing index can be expressed as follows:

$$G_{f,S}\left(SFRC\right)=1.321\left(\frac{V_f L_f}{\phi_f}\right)^{0.135}G_{f,S}\left(PC\right) \tag{14}$$

The IFE increased with the strain rate. Therefore, by substituting the DIF in Equations (3) and (4) into Equation (14), the dynamic IFE can be obtained in Equation (15). Figure 13 shows the comparison between the predicted and experimental results. The predicted results are consistent with the experimental data and the mean ratio of the predicted results to the test results is 0.7407 with the corresponding coefficient of variation (COV) of 0.17.

$$G_{f,D}\left(SFRC\right)=DIF_{G_f}G_{f,S}\left(SFRC\right) \quad (15)$$

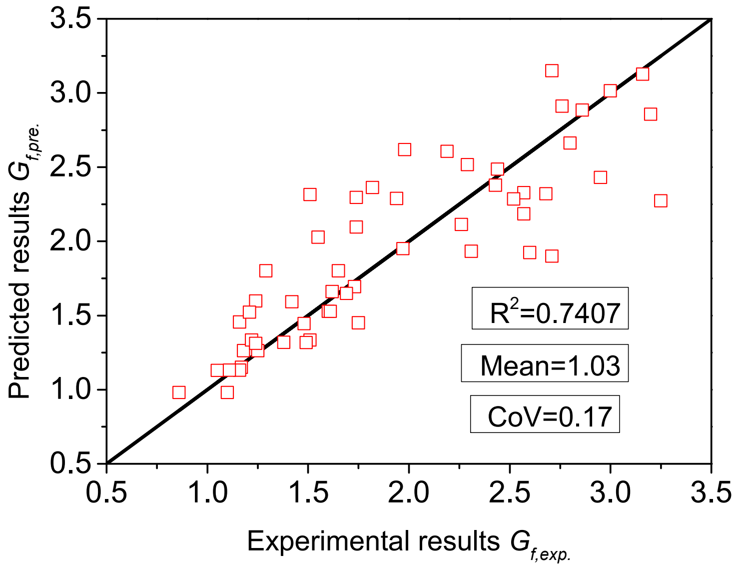

Figure 13. Experimental vs predicted interfacial fracture energy

4.3 Dynamic debonding strain

The single-lap shear test is used to simulate the intermediate crack (IC) induced interfacial debonding in the FRP-strengthened concrete structures. Due to the FRP debonding, only 30%-40% of FRP strength is utilized [50]. Numerous debonding strain models have been proposed for design purpose [51]. However, there is no debonding strain model available considering FRP-strengthened SFRC elements and strain rate effect. Therefore, an empirical debonding strain model by incorporating steel fibre volume and strain rate is proposed in this study. Using the model proposed by JSCE [52], the proposed IFE by incorporating the steel fibre volume and strain rate expressed in Equation (15) can be used to obtain the ultimate debonding strain in Equation (16). The predicted results are in good agreement with the experimental data, as shown in Figure 14. The mean ratio of the predicted results to the experimental results was 0.97, and the corresponding coefficient of variation (COV) was 0.059.

$$\varepsilon_{u,D} = \sqrt{\frac{2G_{f,D}}{E_f t_f}} \tag{16}$$

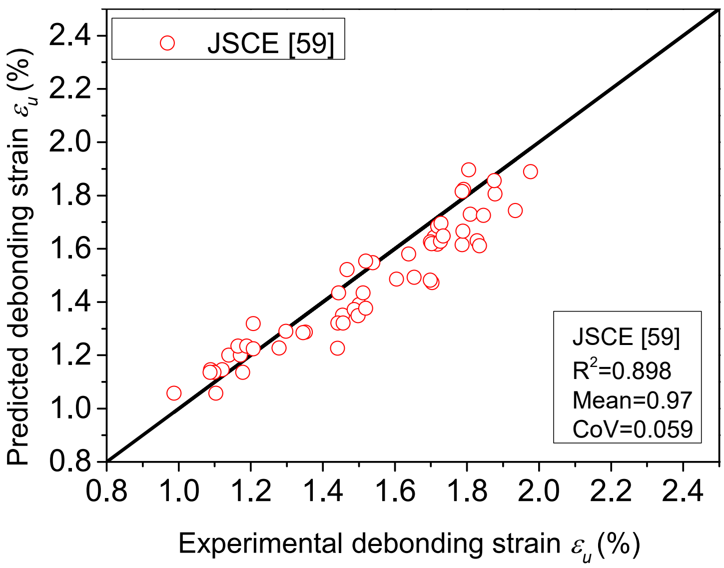

Figure 14. Experimental vs predicted debonding strain

4.4 Dynamic peak shear stress and slip

The interfacial PSS is obtained from the strain distributions. Based on the test results of the present study, the PSS increased slightly with steel fibre volume and increased significantly with strain rate. There is a consistent finding that the interfacial shear stress is determined by f_t and β_w [53, 54]. Therefore, the formula to predict the static PSS can be expressed as follows:

$$\tau_{m,s}\left(PC\right) = 0.646\beta_w\sqrt{f_t} \tag{17}$$

The interfacial PSS increased with the steel fibre volume. Therefore, the fibre-reinforcing index ($V_f L_f/\phi_f$) should be a factor determining the PSS of the BFRP-SFRC interface. Based on the best-fit coefficients from regression analysis, the interfacial PSS can be expressed by the fibre-reinforcing index in the following way:

$$\tau_{m,s}\left(SFRC\right) = 1.421\left(\frac{V_f L_f}{\phi_f}\right)^{0.17}\tau_{m,s}\left(PC\right) \tag{18}$$

The interfacial PSS increased with the rising strain rate. Therefore, by substituting the DIF in Equations (5) and (6) into Equation (18), the dynamic interfacial PSS in Equation (19) can be obtained. Figure 15 shows the comparison between the predicted and experimental results. The predicted results are in good agreement with the test data as the ratio between the predicted and test results is 1.03 and the corresponding coefficient of variation (COV) is 0.14.

$$\tau_{m,D}\left(SFRC\right) = DIF_{\tau_{m,s}} \tau_{m,s}\left(SFRC\right) \tag{19}$$

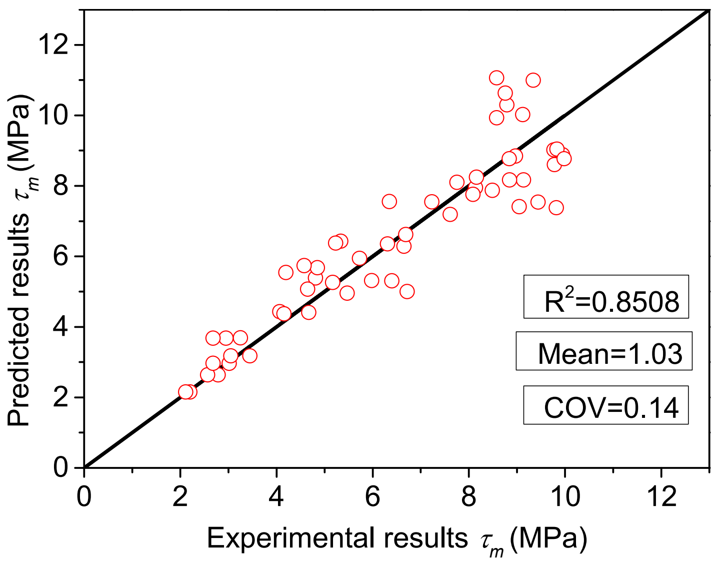

Figure 15. Experimental vs predicted interfacial peak shear stress

The maximum elastic slip s_1 is the maximum slip corresponding to the elastic stage of the bond-slip curves. The elastic slip is mainly resulted from the shear deformation within the bonded region. The elastic slip slightly decreased with the increasing strain rate, but results were less consistent and presented higher scatter. As a result, the elastic shear slip was set as a constant of 0.13 mm for simplicity.

4.5 Analysis and validation of the dynamic bond-slip model

Figure 16 shows the comparisons between the model predictions based on Equations (7) to (19) and the directly measured experimental results for the strain-slip response and bond-slip response. Based on the obtained parameters τ_m, s_1, and ω, the predicted strain-slip and bond-slip relationships are in good agreement with the test data. This comparison demonstrates that the proposed bond-slip models can accurately predict the dynamic interfacial bond-slip of BFRP-to-SFRC interface. Figure 17 illustrates the comparison between the experimental and tested debonding load. The debonding load can be obtained by a widely accepted formula $P_u = b_f \sqrt{2E_f t_f G_f}$ [55] with the strain rate effect included in the corresponding dynamic interfacial fracture energy. As shown the predictions agree well with the test data, with a mean value of 1.013 and a *COV* of 0.08.

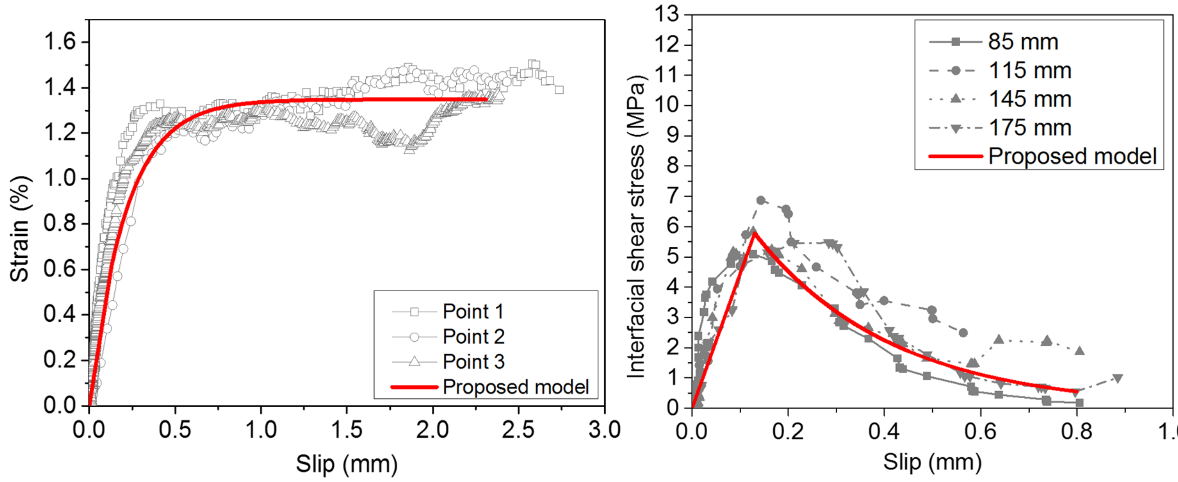

(a) Strain-slip response of D0.5-1-1 (b) Bond-slip response of D0.5-1-1

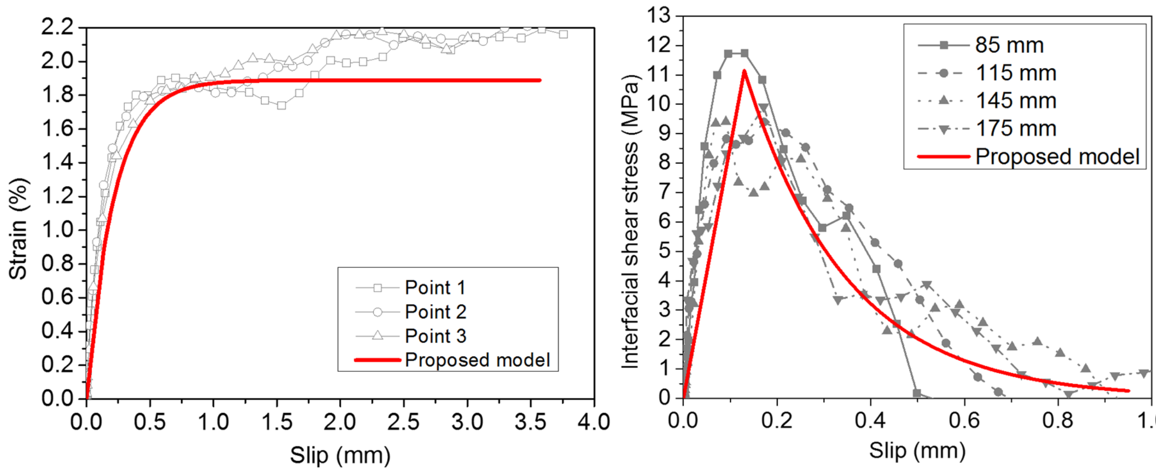

(c) Strain-slip response of D1.5-8-1 (d) Bond-slip response of D1.5-8-1

Figure 16. Comparisons of analytical predictions and tests data of strain-slip curve and bond-slip curve

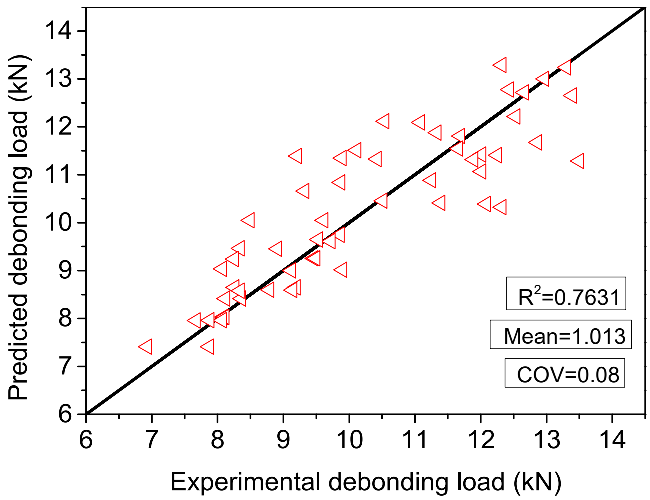

Figure 17. Experimental vs predicted debonding load

5. Conclusions

This study investigated the dynamic interfacial bond behaviour of BFRP-to-SFRC interface. The single-lap shear test method was used to evaluate the bond strength and bond-slip relationships. The following conclusions can be drawn:

(1) Strain rate had a significant effect on the debonding failure modes. With the increasing strain rate, the damage mode shifted the debonding area from concrete layer to the concrete-epoxy interface. When the damage mode changed to concrete-epoxy interface, adding steel fibres had only limited improvement on the debonding load.

(2) The addition of steel fibres increased the debonding load due to the improved microcracking resistant capacity of SFRC substrate. Additionally, the strain rate had more significant effect on the debonding load than the enhanced tensile strength of SFRC by adding steel fibre.

(3) The addition of steel fibres resulted in higher IFE as the large fracture area dissipated more fracture energy. In addition, the IFE increased with strain rate as the shear resistance was enhanced under high loading rate.

(4) The addition of steel fibres resulted in higher interfacial shear stress due to the enhanced bond strength. In addition, strain rate had significant effect on the PSS as the ultimate debonding strain of BFRP increased with strain rate.

(5) The addition of steel fibres and strain rate had nearly no effect on the pattern of bond-slip relationship, i.e. ascending and descending branches, which were similar to the control specimen. However, the IFE increased with increase of steel fibres and the rising strain rate.

(6) Empirical bond-slip model was proposed by incorporating the strain rate effect. The proposed model gave good predictions of the experimental results.

Acknowledgement

The authors acknowledge the financial support from Australian Research Council (ARC LP150100259).

References

[1] A.A. Mutalib, H. Hao. Development of Pi Diagrams for Frp Strengthened Rc Columns. International journal of impact engineering 38 (5) (2011) 290-304.
[2] M. Saatcioglu, T. Ozbakkaloglu, N. Naumoski, A. Lloyd. Response of Earthquake-Resistant Reinforced-Concrete Buildings to Blast Loading. Canadian Journal of Civil Engineering 36 (8) (2009) 1378-90.
[3] S. Lan, T.-S. Lok, L. Heng. Composite Structural Panels Subjected to Explosive Loading. Constr Build Mater 19 (5) (2005) 387-95.
[4] J.-Y. Lee, H.-O. Shin, K.-H. Min, Y.-S. Yoon. Flexural Assessment of Blast-Damaged Rc Beams Retrofitted with Cfrp Sheet and Steel Fiber. International Journal of Polymer Science 2018 (2018).
[5] S.T. Smith, J. Teng. Frp-Strengthened Rc Beams. I: Review of Debonding Strength Models. Eng Struct 24 (4) (2002) 385-95.
[6] B. Wan, C. Jiang, Y.-F. Wu. Effect of Defects in Externally Bonded Frp Reinforced Concrete. Constr Build Mater 172 (2018) 63-76.
[7] T.M. Pham, H. Hao. Impact Behavior of Frp-Strengthened Rc Beams without Stirrups. J Compos Constr 20 (4) (2016) 04016011.
[8] E. Monaldo, F. Nerilli, G. Vairo. Effectiveness of Some Technical Standards for Debonding Analysis in Frp-Concrete Systems. Compos B Eng 160 (2019) 254-67.
[9] W. Chen, T.M. Pham, H. Sichembe, L. Chen, H. Hao. Experimental Study of Flexural Behaviour of Rc Beams Strengthened by Longitudinal and U-Shaped Basalt Frp Sheet. Compos B Eng 134 (2018) 114-26.

[10] J. Teng, S.T. Smith, J. Yao, J.F. Chen. Intermediate Crack-Induced Debonding in Rc Beams and Slabs. Constr Build Mater 17 (6) (2003) 447-62.
[11] Y. Wu, Z. Zhou, Q. Yang, W. Chen. On Shear Bond Strength of Frp-Concrete Structures. Eng Struct 32 (3) (2010) 897-905.
[12] Z. Wang, J. Wu, J. Wang. Experimental and Numerical Analysis on Effect of Fibre Aspect Ratio on Mechanical Properties of Srfc. Constr Build Mater 24 (4) (2010) 559-65.
[13] J. Thomas, A. Ramaswamy. Mechanical Properties of Steel Fiber-Reinforced Concrete. J Mater Civil Eng 19 (5) (2007) 385-92.
[14] L. Li, Y. Guo, F. Liu. Test Analysis for Frc Beams Strengthened with Externally Bonded Frp Sheets. Constr Build Mater 22 (3) (2008) 315-23.
[15] J. Yin, Z.S. Wu. Structural Performances of Short Steel-Fiber Reinforced Concrete Beams with Externally Bonded Frp Sheets. Constr Build Mater 17 (6-7) (2003) 463-70.
[16] S.S. Ibrahim, S. Eswari, T. Sundararajan. Experimental Investigation on Frc Beams Strengthened with Gfrp Laminates. Electronic Journal of Structural Engineering 15 (2015) 1.
[17] V. Gribniak, V. Tamulenas, P.-L. Ng, A.K. Arnautov, E. Gudonis, I. Misiunaite. Mechanical Behavior of Steel Fiber-Reinforced Concrete Beams Bonded with External Carbon Fiber Sheets. Materials 10 (6) (2017) 666.
[18] E. Benvenuti, N. Orlando. Failure of Frp-Strengthened Sfrc Beams through an Effective Mechanism-Based Regularized Xfem Framework. Compos Struct 172 (2017) 345-58.
[19] D. Shen, Y. Ji, F. Yin, J. Zhang. Dynamic Bond Stress-Slip Relationship between Basalt Frp Sheet and Concrete under Initial Static Loading. J Compos Constr 19 (6) (2015) 04015012.
[20] J. Huo, J. Liu, X. Dai, J. Yang, Y. Lu, Y. Xiao, G. Monti. Experimental Study on Dynamic Behavior of Cfrp-to-Concrete Interface. J Compos Constr 20 (5) (2016) 04016026.
[21] J.W. Shi, H. Zhu, Z.S. Wu, G. Wu. Experimental Study of the Strain Rate Effect of Frp Sheet-Concrete Interface. China Civil Eng J 45 (12) (2012) 99-107.
[22] P. Buchan, J. Chen. Blast Resistance of Frp Composites and Polymer Strengthened Concrete and Masonry Structures–a State-of-the-Art Review. Compos B Eng 38 (5-6) (2007) 509-22.
[23] C. Yuan, W. Chen, T.M. Pham, H. Hao. Bond Behavior between Basalt Fibres Reinforced Polymer Sheets and Steel Fibres Reinforced Concrete. Eng Struct 176 (2018) 812-24.
[24] W. Chen, H. Hao, M. Jong, J. Cui, Y. Shi, L. Chen, T.M. Pham. Quasi-Static and Dynamic Tensile Properties of Basalt Fibre Reinforced Polymer. Compos B Eng 125 (2017) 123-33.
[25] N. Taniguchi, T. Nishiwaki, N. Hirayama, H. Nishida, H. Kawada. Dynamic Tensile Properties of Carbon Fiber Composite Based on Thermoplastic Epoxy Resin Loaded in Matrix-Dominant Directions. Composites Science and Technology 69 (2) (2009) 207-13.
[26] W. Chen, F. Lu, M. Cheng. Tension and Compression Tests of Two Polymers under Quasi-Static and Dynamic Loading. Polymer testing 21 (2) (2002) 113-21.
[27] W. Chen, H. Hao, D. Hughes, Y. Shi, J. Cui, Z.-X. Li. Static and Dynamic Mechanical Properties of Expanded Polystyrene. Materials & Design 69 (2015) 170-80.
[28] Y. Xia, J. Zhu, K. Wang, Q. Zhou. Design and Verification of a Strain Gauge Based Load Sensor for Medium-Speed Dynamic Tests with a Hydraulic Test Machine. International Journal of Impact Engineering 88 (2016) 139-52.
[29] H.C. Biscaia, C. Chastre, I.S. Borba, C. Silva, D. Cruz. Experimental Evaluation of Bonding between Cfrp Laminates and Different Structural Materials. J Compos Constr 20 (3) (2015) 04015070.

[30] C. Yuan, W. Chen, T.M. Pham, H. Hao. Effect of Aggregate Size on Bond Behaviour between Basalt Fibre Reinforced Polymer Sheets and Concrete. Compos B Eng 158 (2019) 459-74.
[31] D. Zhang, X.-L. Gu, Q.-Q. Yu, H. Huang, B. Wan, C. Jiang. Fully Probabilistic Analysis of Frp-to-Concrete Bonded Joints Considering Model Uncertainty. Compos Struct 185 (2018) 786-806.
[32] M. Ali-Ahmad, K. Subramaniam, M. Ghosn. Experimental Investigation and Fracture Analysis of Debonding between Concrete and Frp Sheets. J Eng Mech 132 (9) (2006) 914-23.
[33] R. Olivito, F. Zuccarello. An Experimental Study on the Tensile Strength of Steel Fiber Reinforced Concrete. Compos B Eng 41 (3) (2010) 246-55.
[34] X. Zhou, H. Hao. Modelling of Compressive Behaviour of Concrete-Like Materials at High Strain Rate. Int J Solids Struct 45 (17) (2008) 4648-61.
[35] Y. Hao, H. Hao, G. Jiang, Y. Zhou. Experimental Confirmation of Some Factors Influencing Dynamic Concrete Compressive Strengths in High-Speed Impact Tests. Cement Concrete Res 52 (2013) 63-70.
[36] H. Ko, S. Matthys, A. Palmieri, Y. Sato. Development of a Simplified Bond Stress–Slip Model for Bonded Frp–Concrete Interfaces. Constr Build Mater 68 (2014) 142-57.
[37] Y.-F. Wu, X.-S. Xu, J.-B. Sun, C. Jiang. Analytical Solution for the Bond Strength of Externally Bonded Reinforcement. Compos Struct 94 (11) (2012) 3232-9.
[38] M. Perrella, V. Berardi, G. Cricrì. A Novel Methodology for Shear Cohesive Law Identification of Bonded Reinforcements. Compos B Eng 144 (2018) 126-33.
[39] S. Liu, H. Yuan, J. Wu. Full-Range Mechanical Behavior Study of Frp-to-Concrete Interface for Pull-Pull Bonded Joints. Compos B Eng 164 (2019) 333-44.
[40] A. Caggiano, E. Martinelli, D.S. Schicchi, G. Etse. A Modified Duvaut-Lions Zero-Thickness Interface Model for Simulating the Rate-Dependent Bond Behavior of Frp-Concrete Joints. Compos B Eng 149 (2018) 260-7.
[41] J. He, G. Xian. Bond-Slip Behavior of Fiber Reinforced Polymer Strips-Steel Interface. Constr Build Mater 155 (2017) 250-8.
[42] Y.-W. Zhou, Y.-F. Wu, Y. Yun. Analytical Modeling of the Bond–Slip Relationship at Frp-Concrete Interfaces for Adhesively-Bonded Joints. Compos B Eng 41 (6) (2010) 423-33.
[43] Y.-F. Wu, C. Jiang. Quantification of Bond-Slip Relationship for Externally Bonded Frp-to-Concrete Joints. J Compos Constr 17 (5) (2013) 673-86.
[44] J. Dai, T. Ueda, Y. Sato. Bonding Characteristics of Fiber-Reinforced Polymer Sheet-Concrete Interfaces under Dowel Load. J Compos Constr 11 (2) (2007) 138-48.
[45] H.-T. Wang, G. Wu. Bond-Slip Models for Cfrp Plates Externally Bonded to Steel Substrates. Compos Struct 184 (2018) 1204-14.
[46] D. Shen, H. Shi, Y. Ji, F. Yin. Strain Rate Effect on Effective Bond Length of Basalt Frp Sheet Bonded to Concrete. Constr Build Mater 82 (2015) 206-18.
[47] H. Toutanji, P. Saxena, L. Zhao, T. Ooi. Prediction of Interfacial Bond Failure of Frp–Concrete Surface. J Compos Constr 11 (4) (2007) 427-36.
[48] Y. Yun, Y.-F. Wu, W.C. Tang. Performance of Frp Bonding Systems under Fatigue Loading. Eng Struct 30 (11) (2008) 3129-40.
[49] Y. Yun, Y.-F. Wu. Durability of Cfrp–Concrete Joints under Freeze–Thaw Cycling. Cold Regions Science and Technology 65 (3) (2011) 401-12.
[50] F.M. Mukhtar, R.M. Faysal. A Review of Test Methods for Studying the Frp-Concrete Interfacial Bond Behavior. Constr Build Mater 169 (2018) 877-87.
[51] X. Huang, L. Sui, F. Xing, Y. Zhou, Y. Wu. Reliability Assessment for Flexural Frp-Strengthened Reinforced Concrete Beams Based on Importance Sampling. Compos B Eng 156 (2019) 378-98.

[52] K. Maruyama, T. Ueda. Jsce Recommendations for Upgrading of Concrete Structures with Use of Continuous Fiber Sheets. FRP Composites in Civil Engineering Proceedings of the International Conference on FRP composites in Civil EngineeringHong Kong Institution of Engineers, Hong Kong Institution of Steel Construction2001.
[53] X.Z. Lu, J.G. Teng, L.P. Ye, J.J. Jiang. Bond–Slip Models for Frp Sheets/Plates Bonded to Concrete. Eng Struct 27 (6) (2005) 920-37.
[54] H. Ko, Y. Sato. Bond Stress–Slip Relationship between Frp Sheet and Concrete under Cyclic Load. J Compos Constr 11 (4) (2007) 419-26.
[55] C. Jiang, B. Wan, J. Omboko. Enhancing Frp-to-Concrete Bond Behavior by Epoxy Ribs. Special Publication 327 (2018) 25.1-.14.